

Copyright (2010) American Institute of Physics. This article may be downloaded for personal use only. Any other use requires prior permission of the author and the American Institute of Physics.

The following article appeared in the American Institute of Physics, Journal of Chemical Physics, Vol. 133 164312 (2010) and may be found at: <http://dx.doi.org/10.1063/1.3475564>.

Global potential energy surfaces for $O(^3P)+H_2O(^1A_1)$ collisions

Patrick F. Conforti,¹ Matthew Braunstein,¹ Bastiaan J. Braams,^{2,a)} and Joel M. Bowman²

¹*Spectral Sciences, Inc., 4 Fourth Ave., Burlington, Massachusetts 01803, USA*

²*Department of Chemistry and Cherry L. Emerson Center for Scientific Computation, Emory University, Atlanta, Georgia 30322, USA*

(Received 26 May 2010; accepted 14 July 2010; published online 27 October 2010)

Global analytic potential energy surfaces for $O(^3P)+H_2O(^1A_1)$ collisions, including the OH+OH hydrogen abstraction and H+OOH hydrogen elimination channels, are presented. *Ab initio* electronic structure calculations were performed at the CASSCF+MP2 level with an $O(4s3p2d1f)/H(3s2p)$ one electron basis set. Approximately 10^5 geometries were used to fit the three lowest triplet adiabatic states corresponding to the triply degenerate $O(^3P)+H_2O(^1A_1)$ reactants. Transition state theory rate constant and total cross section calculations using classical trajectories to collision energies up to $120 \text{ kcal mol}^{-1}$ ($\sim 11 \text{ km s}^{-1}$ collision velocity) were performed and show good agreement with experimental data. Flux-velocity contour maps are presented at selected energies for H_2O collisional excitation, OH+OH, and H+OOH channels to further investigate the dynamics, especially the competition and distinct dynamics of the two reactive channels. There are large differences in the contributions of each of the triplet surfaces to the reactive channels, especially at higher energies. The present surfaces should support quantitative modeling of $O(^3P)+H_2O(^1A_1)$ collision processes up to $\sim 150 \text{ kcal mol}^{-1}$.

© 2010 American Institute of Physics. [doi:10.1063/1.3475564]

I. INTRODUCTION

Collisions of $O(^3P)$ atom with $H_2O(^1A_1)$ have been observed in many space experiments. At altitudes above $\sim 150 \text{ km}$, $O(^3P)$ begins to become the dominant constituent of the rarefied atmosphere. Collisions between $O(^3P)$ and H_2O from Space Shuttle engine exhaust and H_2O from surface outgassing give rise to rich optical spectra from the long-wave infrared ($\sim 20\text{--}10 \mu\text{m}$) (Ref. 1) through the middle of the infrared ($\sim 10\text{--}1 \mu\text{m}$) (Refs. 2 and 3) to the ultraviolet ($\sim 0.3 \mu\text{m}$),⁴ encompassing pure rotational, rovibrational, and electronic excitation, respectively. Because of the large mean free paths and high relative collision speeds of 8 km s^{-1} ($64.8 \text{ kcal mol}^{-1}$) and greater, these space measurements can be thought of as hyperthermal crossed beam experiments on a large scale. Direct collisional excitation of H_2O , hydrogen abstraction to form OH+OH ($\Delta H_0 = 15.8 \text{ kcal mol}^{-1}$) (Ref. 5) with a $\sim 1\text{--}2 \text{ kcal mol}^{-1}$ barrier, and hydrogen elimination to form H+OOH ($\Delta H_0 = 53.4 \text{ kcal mol}^{-1}$) (Ref. 6) with an observed threshold of $60 \pm 2 \text{ kcal mol}^{-1}$ (Ref. 7) could all play a role in the observed radiation. Ground-based molecular beam⁸ and shock tube experiments⁹ have also observed similar radiation from $O(^3P)+H_2O$ collisions. Recently, Brunsvold *et al.*⁷ have measured and modeled this system at hyperthermal collision velocities of 8 km s^{-1} and higher, focusing on the H+OOH channel dynamics and the competition with the OH+OH channel. The competition of hydrogen abstraction and

elimination has also been observed in $O(^3P)+CH_4$ (Ref. 10) and $O(^3P)+NH_3$ (Ref. 11) collisions and seems to be common in hyperthermal $O(^3P)$ chemistry.

In our previous modeling of the $O(^3P)+H_2O$ system,¹² we fit the three lowest triplet adiabatic potential energy surfaces leading to OH+OH products based on *ab initio* electronic structure calculations. The surfaces were spline-based fits of $\sim 20\,000$ fixed geometry *ab initio* calculations at the complete active space self-consistent field+second order perturbation theory (CASSCF+MP2) level with an $O(4s3p2d1f)/H(3s2p)$ one electron basis set. We also performed classical dynamics calculations for a range of hyperthermal velocities and computed rate constants to form OH+OH. This work suggested that a significant amount of the observed infrared radiation following hyperthermal $O(^3P)+H_2O$ collisions was due to highly rovibrationally excited OH. This OH radiation was in addition to the expected direct collisional excitation of H_2O by $O(^3P)$, modeled in earlier theoretical work.^{2,13}

The work of Karkach and Osherov¹⁴ has shown that collisions of $O(^3P)+H_2O$ take place on a global triplet H_2O_2 potential surface, which plays a significant role in hydrogen-oxygen combustion. On this surface, there are 12 bimolecular reactions formally possible between four channels at low collision energies: H_2+O_2 , $O+H_2O$, OH+OH, and H+OOH. This comprehensive work determined transition states and rate constants for many relevant reactions and showed how these channels connected. However, all these efforts have not yet produced a quantitative description of observed radiation in space and ground experiments from detailed knowledge of the potential surfaces, nor in many cases have basic mechanisms been definitely identified.

The present paper extends our previous work on deter-

^{a)}Present address: Nuclear Data Section, NAPC Division, IAEA, Vienna, Austria.

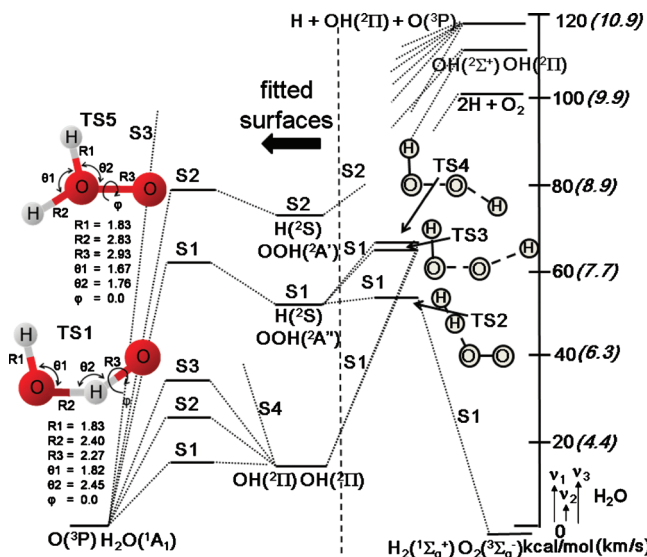
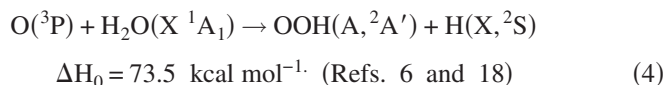
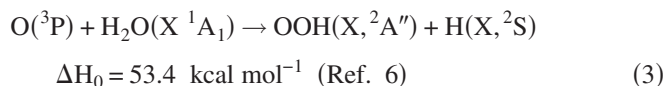
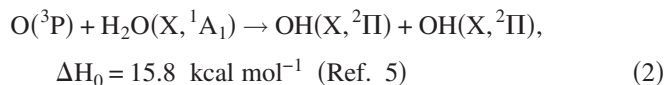
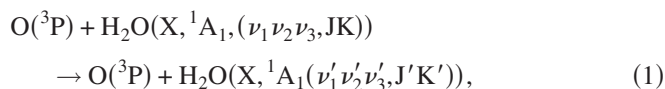


FIG. 1. Energy level diagram of the three lowest triplet electronic states of the $O(^3P)+H_2O(^1A_1)$ system. The fitted surfaces examined in this work are indicated to the left of the vertical dashed line. The geometries of the transition structures TS1 and TS5 are given in atomic units and radians.

mining global analytic potential energy surfaces for $O(^3P)+H_2O$ collisions to include both the $OH+OH$ and $H+OOH$ reactive channels. Calculations were performed again at the CASSCF+MP2 level with an $O(4s3p2d1f)/H(3s2p)$ one electron basis set using the GAMESS electronic structure code.¹⁵ Approximately 10^5 geometries were used to fit the three lowest triplet adiabatic states corresponding to the triply degenerate $O(^3P)+H_2O(^1A_1)$ reactants, compared to $\sim 20\,000$ geometries in our previous work. To fit the *ab initio* points, the method of Bowman and co-workers^{16,17} was used, which includes all nuclear degrees of freedom, and where the interchangeability of like-atoms is built into the functional form of the potential. The following excitation and reactive processes were included



The third surface leading to $OOH(B)+H$, with an excitation energy of $\sim 192.9 \text{ kcal mol}^{-1}$,^{6,18} was too high in energy and was not followed to products.

An overview of the surfaces addressed in the present work is shown in Fig. 1. The energy zero corresponds to separated $O+H_2O$ reactants and includes zero-point energy. The left side of the figure shows the reactants, products, and transition states for reactions (2)–(4) above. Only overall

triplet electronic states are shown. In the figure, S1, S2, and S3 refer to the first three triplet adiabatic electronic surfaces which are degenerate in the $O+H_2O$ separated reactants, following the notation of Ref. 12. The labels TS1–TS5 refer to transition states, following the nomenclature of Ref. 14, and have a similar geometry for each of the three triplet surfaces. On the right side of the figure we show reaction paths to other transition states and to H_2+O_2 products, based on the work of Karkach and Osherov for the lowest triplet surface, S1, as well as other product channels which are not directly addressed by surfaces fit in the present work. The work of Karkach and Osherov¹⁴ and Brunsvold *et al.*⁷ indicates that the $O+H_2O$ path to H_2+O_2 through an $H+OOH$ intermediate (TS2) is unlikely, at least for the lowest triplet surface. Above 11 km s^{-1} ($\sim 120 \text{ kcal mol}^{-1}$), Brunsvold *et al.* determined fragmentation cross sections of the $H+OOH$ product channel leading to $2H(^2S)+O_2(^3\Sigma_g^-)$ and $H(^2S)+OH(^2\Pi)+O(^3P)$ from B3LYP direct dynamics calculations.

In fitting the surfaces, we also included geometries leading to these fragments, but our main focus is with energies below $120 \text{ kcal mol}^{-1}$, and so we have not yet fully evaluated our surface fits for OOH fragmentation. Also, we did not investigate or explicitly fit the conical intersection leading to the $OH(X)+OH(A)$ products.¹⁹ As this electronically excited channel opens at higher collision velocities, we would expect some decrease of the $OH(X)+OH(X)$ and $H+OOH$ reactive cross sections from the present results. At lower collision velocities, a family of singlet surfaces associated with singlet O -atom, $O(^1D)+H_2O(^1A_1)$, and leading to $OH(^2\Pi)+OH(^2\Pi)$ and $H(^2S)+OOH(^2A'')$ (Ref. 20) certainly cross the $O(^3P)+H_2O(^1A_1)$ derived triplet surfaces investigated in the present work. Recent studies on the smaller but similar $O(^3P, ^1D)+H_2$ system found intersystem crossing to have a negligible effect on reaction probabilities.²¹ In addition, for the spin changing reaction $O(^1D)+H_2O(^1A_1) \rightarrow O(^3P)+H_2O(^1A_1)$, Ref. 22 measures a product branching ratio of 0.02 ± 0.01 at room temperature, a relatively small value. Given these facts, the reasonable level of agreement with experimental data using the present triplet only surfaces, and the good agreement with experimental data for $O(^1D)+H_2O(^1A_1)$ reactions using a singlet surface in Ref. 20, electronic coupling between triplet and singlet surfaces is probably small. However, an explicit treatment of this singlet-triplet coupling has yet to be done. Apart from these considerations, we judge the quality of our present fitted surfaces to be very good from the $O+H_2O$ threshold to about $150 \text{ kcal mol}^{-1}$. Above this energy the quality of the fits begins to fall off and fragmentation of the OOH product probably becomes increasingly important. Therefore taken together, we believe the present surfaces should be able to quantitatively model $O+H_2O$ collision processes from threshold to $\sim 120 \text{ kcal mol}^{-1}$ and probably up to $150 \text{ kcal mol}^{-1}$.

The main goal of the present paper is to give the details of these fitted surfaces and to assess their quality for future in depth dynamical studies. As part of this assessment, we used variational transition state theory with the present surfaces to compute rate constants leading to $OH+OH$ and $H+OOH$, which compare favorably to available measurements. We

have also computed total cross sections using quasiclassical trajectories (QCTs) for production of OH+OH and H+OOH from 4 to 11 km s⁻¹ (16.2 to 122.5 kcal mol⁻¹). We compared these results to our previous work which did not include the H+OOH channel¹² and to the measurements and direct dynamics modeling results of Brunsvold *et al.*⁷ For the OH+OH channel, the present results are about a factor of 4 lower than those reported by Brunsvold *et al.* using B3LYP density functional direct dynamics on a single surface and about a factor of 2 lower than our previous results¹² which used fitted surfaces only for the OH+OH channel. For the H+OOH channel, the present results are about a factor of 5 larger than the B3LYP direct dynamics cross sections of Brunsvold *et al.*⁷ at threshold and are nearly same at 120 kcal mol⁻¹. The present H+OOH results have good agreement with molecular beam measurements⁷ for the relative cross section. In all these calculations, each surface is considered independently, and electronic and spin-orbit coupling to nearby singlet surfaces is not considered. We have also computed flux-velocity contour maps at selected energies for H₂O collisional excitation, OH+OH, and H+OOH to further investigate the dynamics, especially the competition between OH+OH and H+OOH. Even in such a small and elementary system, the dynamics of these two channels are different and give rise to distinctly different angular distributions. We find large differences in the contributions of each of the electronic triplet surfaces, especially at higher energies where the OH+OH and H+OOH channels are competitive. It is hoped that these initial results may be a useful guide for future hyperthermal measurements of these quantities.

The paper proceeds as follows. Section II describes the *ab initio* electronic structure calculations, the fitting of the potential energy surfaces, and some general properties of the fitted surfaces. Section III describes the rate constant calculations and QCT calculations for the OH+OH and H+OOH channels. Section IV gives conclusions.

II. FITTING THE POTENTIAL SURFACES

A. *Ab initio* calculations

To achieve high accuracy, the CASSCF+MP2 theory was used within the GAMESS computational chemistry package.¹⁵ These calculations are performed using a ten electron, eight orbital CASSCF, or CASSCF[10, 8]. The triple zeta valence (TZV) (4s3p) basis set of GAMESS plus two *d* and one *f* functions on the oxygens and two *p* functions on the hydrogens were used (O(4s3p2d1f)/H(3s2p)) for a total of 90 basis functions. The CASSCF[10e8o] includes excitations within the space of two bonding, two lone pair, two singly occupied, and two unoccupied antibonding orbitals. (The 1s and 2s oxygen orbitals are not included in the CASSCF space.) For the MP2 calculation, all orbitals are included, except the 1s oxygen cores. The active space was chosen in order to ensure that the proper orbitals were included to characterize the reactant and product states and bond breaking and formation. The three lowest triplet electronic states for the combined O(³P)+H₂O(¹A₁) system are

state averaged, so that the separated reactants are energetically degenerate.

An overview of the potential energy surfaces for the O(³P)+H₂O(¹A₁) collision system is given on left side of Fig. 1. The transition states TS1 and TS5 are particularly important as well as the product states OH(²Π)+OH(²Π) and H(²S)+OOH(²A). The energy scale on the right of the figure is given in kcal mol⁻¹ and km s⁻¹ O+H₂O collision velocity in parentheses, with the H₂O fundamental vibrational energies drawn as arrow heights for reference. Previous calculations¹⁴ have determined geometries of the lowest triplet electronic state of these transition structures, which are used as starting points for building a large database of geometries for fitting the surfaces. The database was constructed in the following way. Given the structure TS1 in Fig. 1, R1 was held constant at 1.83 a.u. while R2 and R3 were individually varied from 1.13 to 8.69 a.u. with steps of 0.76 a.u. The angles θ₁ and θ₂ were varied from 0.873 to 5.585 rad with a step size of 0.523 rad. The dihedral angle φ was varied from 0 to 3.14 rad with a step size of 0.523 rad. Similarly for TS5 in Fig. 1, R1 was fixed at 1.83 a.u. while R2 and R3 were varied from 1.13 to 8.69 a.u. with steps of 0.76 a.u. The angles θ₁ and θ₂ were varied from 0.873 to 2.967 radians with a step size of 0.523 rad, and the torsion angle φ was varied from 0 to 3.14 rad with a step size of 0.523 rad. This set of points provides adequate sampling of the TS1 and TS5 regions. While the vast majority of electronic structure calculations at these geometries converged, some structures with O–O internuclear distances less than 1.89 a.u. did not, and they are excluded from the fitted surface.

Geometries closely related to the reactant and product states were examined using a coarser set of *ab initio* points. For the initial reactant state, the H₂O minimum geometry of Partridge and Schwenke was used²³ as a starting point, where the H–O–H bond angle is 1.827 rad and each OH bond length is 1.812 a.u. With this reactant H₂O geometry fixed, the attacking atomic oxygen is set at distances of 7.56–17.0 a.u. from the oxygen of the H₂O molecule, and the H₂O orientation is randomized using Euler's angles. The H₂O H–O–H bond angle is then varied from 1.04 to 3.14 rad with a step size of 0.698 rad, and the O–H bond lengths of H₂O are varied from 1.51 to 3.02 a.u. with a step size of 0.76 a.u. Approximately ten randomized orientations between the O and H₂O are used for each set of H₂O coordinates. A similar procedure was used to sample the H+OOH product state. The geometry of Ref. 24 was used as a starting point for the OOH product, where the O–O–H angle is 1.82 rad, the H–O bond distance is 1.83 a.u., and the O–O bond distance is 2.51 a.u. In this case, the eliminating hydrogen is set at distances of 7.56–17.0 a.u. from the center oxygen of the OOH molecule, and the OOH orientation with respect to the eliminating hydrogen is randomized using Euler's angles. The internal OOH angles and O–H bond lengths examined are the same as the H₂O reactant case. For the OH+OH product state, the O–H bond length is initially set at 1.85 a.u.²⁵ This bond length is varied from 1.51 to 3.02 a.u. with a step size of 0.76 a.u. The distance between OH molecules

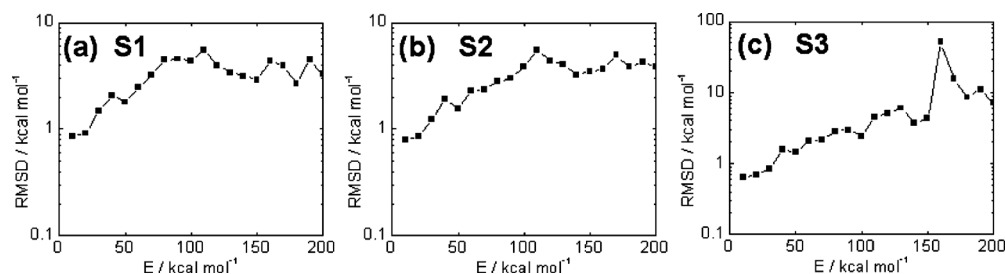


FIG. 2. The RMSD given in kcal mol^{-1} is plotted vs energy bin (kcal mol^{-1}) for (a) the S1 surface, (b) the S2 surface, and (c) the S3 surface.

is varied from 7.56 to 17.0 a.u. and the orientation of each OH molecule is randomized according to Euler's angles.

This initial set of geometries sampling the reactant, OH+OH and H+OOH product spaces, and transition state, TS1 and TS5-like structures, total approximately 95 000 internuclear configurations. These points were initially fit with the procedure described below.^{16,17} The fit was used in several O+H₂O QCT calculations at a number of collision energies. Undersampled areas of the potential surfaces were quickly identified from the QCT calculations and additional geometries were generated and the surfaces were refit. Several iterations of this refitting procedure added approximately 15 000 geometries. Approximately 110 000 separate internuclear configurations were used in the final fits of the surfaces.

B. Potential energy surface fits

Potential energy surfaces were constructed using a functional form and fitting procedure described in detail in Ref. 17. Each of the three lowest triplet electronic states is fit separately. For a particular surface fit, the six internuclear bond distances, r_{ij} , are used, as this facilitates a representation that is invariant with respect to like-nuclei. The basis functions used are functions of auxiliary variables $x_{ij} = \exp(-r_{ij}/a)$. The fits were of the form $p(x)$, where $p(x)$ is polynomial in all the x_{ij} . For $p(x)$ we used a seventh degree polynomial giving a total of approximately 500 terms for each surface.

To assess the quality of the fits, we calculated the root mean square deviation (RMSD) between the fitted potential energy surface (PES) and CASSCF+MP2 energies. Figure 2 shows the RMSD in 10 kcal mol^{-1} energy bins with respect to the O(³P)+H₂O(¹A₁) reactant asymptote. Below the CASSCF+MP2 energy of 50 kcal mol^{-1} , the RMSD is less

than 3 kcal mol^{-1} . The hydrogen abstraction reaction occurs in this energy region of the surface and this small RMSD value insures an accurate dynamics simulation with the fitted PES. Additionally, a quality fit in this low energy region is necessary to characterize the internal energy of inelastically scattered (nonreacted) H₂O in future dynamics simulations. For CASSCF+MP2 energies less than 150 kcal mol^{-1} , the RMSD is less than 10 kcal mol^{-1} . This energy region includes the hydrogen elimination reaction. While there is spike of approximately 50 kcal mol^{-1} in the RMSD on the S3 surface at approximate 160 kcal mol^{-1} , we limit the collision energy to 122.5 kcal mol^{-1} (maximum collision velocity of 11 km s^{-1}) in the simulations described below.

C. Properties of the fitted PESs

The CASSCF-MP2 *ab initio* and fitted PES stationary point energies are given in Tables I and II for the abstraction and elimination channels, respectively. Results are given for the three lowest triplet electronic states, S1, S2, and S3, and compared to literature values. Values in parentheses include zero-point correction. Figure 1 gives the transition state structures of the lowest fitted surface as verified by a single imaginary frequency, and these geometries were used to determine the TS1 and TS5 energies in the Tables for all electronic states. Likewise, the minimum energy reactant H₂O (O–H=O–H=1.814 a.u.; H–O–H=1.94 rad) and product OOH (O–O=2.55 a.u.; O–H=1.85 a.u.; O–O–H=1.72 rad) and OH (O–H=1.85 a.u.) geometries of the lowest triplet fitted surface were used to determine the reaction energies. For the Table I results, we first note that the use of three-state averaging to describe the quadruply degenerate OH+OH products make the ΔE CASSCF+MP2 S1, S2, and S3 energies (and the OH+OH S1, S2, and S3 PES

TABLE I. Stationary point comparison between the fitted PES and the CASSCF+MP2 calculations for the reaction O(³P)+H₂O(¹A₁)→OH(²Π)+OH(²Π). All energies are given in kcal mol^{-1} relative to the O(³P)+H₂O(¹A₁) reactant asymptote. The $\Delta E(\text{TS1})$ columns list energies of TS1 relative to the O+H₂O asymptote. The ΔE columns list energies of the OH+OH product relative to the O+H₂O asymptote. Values in parentheses include zero-point correction. The geometry of the TS1 structure is given in Fig. 1 and is the same for each surface. Literature values are (a) Ref. 14 using QCISD(T)/6-311(d,p)+estimates from larger basis sets, (b) Ref. 7 using CCSD(T)/aug-cc-pVTZ, and (c) Ref. 5 which can be considered as benchmark.

O(³ P)+H ₂ O(¹ A ₁)→OH(² Π)+OH(² Π)						
	PES		CASSCF+MP2		Literature	
	$\Delta E(\text{TS1})$	ΔE	$\Delta E(\text{TS1})$	ΔE	$\Delta E(\text{TS1})$	ΔE
S1	18.5(15.9)	17.0(14.1)	18.0(15.4)	14.9(12.0)	20.1 ^a 21.2(18.0) ^b	18.45 ^a , 18.9(16.1) ^b , (15.8) ^c
S2	26.0(22.9)	16.9(14.0)	24.7(21.6)	14.9(12.0)		
S3	34.8(31.7)	17.9(15.0)	42.2(39.1)	16.3(13.4)		

TABLE II. Stationary point comparison between the fitted PES and the CASSCF+MP2 calculations for the reaction $O(^3P)+H_2O(^1A_1)\rightarrow H(^2S)+OOH(^2A)$. All energies are given in kcal mol⁻¹ relative to the $O(^3P)+H_2O(^1A_1)$ reactant asymptote. The $\Delta E(\text{TS5})$ columns list energies of TS5 relative to the $O+H_2O$ asymptote. The ΔE columns list energies of the $H+OOH$ product relative to the $O+H_2O$ asymptote. Values in parentheses include zero-point correction. The geometry of the TS5 structure is given in Fig. 1 and is the same for the first two surfaces. Literature values are (a) Ref. 14 using QCISD(T)/6-311(d,p)+estimates from larger basis sets, (b) Ref. 7 using CCSD(T)/aug-cc-pVTZ, (c) Ref. 6 which can be considered as benchmark, and (d) Ref. 6 for S1 state+T₀(S2) (20.1 kcal mol⁻¹) (Ref. 18).

O(³ P)+H ₂ O(¹ A ₁)→H(² S)+OOH(² A)						
	PES		CASSCF+MP2		Literature	
	ΔE(TS5)	ΔE	ΔE(TS5)	ΔE	ΔE(TS5)	ΔE
S1	66.0(62.6)	54.0(49.7)	67.8(64.4)	52.8(48.5)	71.2 ^a , 74.3(70.9) ^b	54.9 ^a , 59.4(54.8) ^b , (53.4) ^c
S2	82.7(79.2)	73.8(69.5)	81.4(77.9)	74.3(70.0)	...	(73.5) ^d

energies) slightly different from each other. Referring to the zero-point inclusive values in the Table, the CASSCF+MP2 reaction and transition energies for the S1 state underestimate the best literature values by 2–4 kcal mol⁻¹, with the PES having a larger barrier height than the CASSCF+MP2. However, the difference between the TS1 barrier and OH+OH asymptote of ~2 kcal mol⁻¹ for the S1 PES is in excellent agreement with the best available literature value. The CASSCF+MP2 barrier heights of 21.6 and 39.1 kcal mol⁻¹ for the S2 and S3 surfaces, respectively, clearly show that both S2 and S3 states contribute to the overall OH reactive cross section at collision velocities above ~7 km s⁻¹. The PES energies are consistent with the CASSCF+MP2 values, with the largest error being 7.4 kcal mol⁻¹ for the S3 barrier height.

The fitted surfaces for the hydrogen abstraction reaction are compared with the *ab initio* points in Fig. 3. The potential of the S1, S2, and S3 states are plotted in (a), (b), and (c) for the CASSCF+MP2 calculations and compared with the S1, S2, and S3 states of the fitted PES in (d), (e), and (f). The TS1 geometry from Fig. 1 is used, where R_1 , θ_1 , θ_2 , and φ are fixed while R_2 and R_3 are varied from 1 to 5 a.u. As the values of R_2 increase with $R_3\sim 1.83$ a.u., the O–H₂O complex shifts toward the OH+OH product state, and likewise as the values of R_3 increase with $R_2\sim 1.83$ a.u., the O–H₂O shifts toward the reactant state. In comparing the fitted PES with the *ab initio* surfaces, the general features of the surface are well reproduced by the fit, with the largest errors occurring near the saddle region of the S3 surface. Near the saddle point, the fitted PES underestimates the barrier height. This underestimate would tend to overpredict the reactive cross section on the S3 surface very close to the OH+OH threshold. However, outside of the saddle point region, the fitted PES for the S3 state well reproduces the characteristics of the *ab initio* surface.

For $O(^3P)+H_2O(^1A_1)\rightarrow H(^2S)+OOH(^2A)$, hydrogen elimination, the stationary point energies are given in Table II. While the S3 surface was calculated, no H+OOH product minimum was found. The reaction energy for the S1 surface is 48.5 kcal mol⁻¹ including zero point using CASSCF+MP2 and 49.7 kcal mol⁻¹ including zero point using the PES, which are within 5 kcal mol⁻¹ of the experimental benchmark literature value of 53.4 kcal mol⁻¹.⁶ On the S2 surface, the reaction is more endothermic by 21.5 and 19.8 kcal mol⁻¹ for the CASSCF+MP2 and the fitted PES,

respectively. The *ab initio* and PES reaction energies are within 4 kcal mol⁻¹ of the best literature value for the S2 electronic state.^{6,18} It is interesting that the reaction barriers for the abstraction reaction for all three electronic states are less than the energy threshold for elimination. For the S1 state elimination reaction, the barrier height is 64.4 and 62.6 kcal mol⁻¹ (~8 km s⁻¹) using CASSCF+MP2 and the fitted PES, respectively. This compares to a value of 60 ± 2 kcal mol⁻¹ estimated by Brunsvold *et al.* as indicated by the onset of appearance of OOH product in molecular beam measurements.⁷ The barrier height for the S2 state is 81.4 and 82.7 kcal mol⁻¹ (~9 km s⁻¹) using the CASSCF+MP2 and PES, respectively.

For the elimination reaction, the fitted surfaces are compared with the *ab initio* surfaces near the saddle point in Fig. 4. The S1, S2, and S3 results for the CASSCF+MP2 calculations are shown in (a), (b), and (c) compared to the fitted PES shown in (d), (e), and (f). The transition state geometry given in Fig. 1 is used where R_1 , θ_1 , θ_2 , and φ are fixed while R_3 and R_2 are varied from 1.5 to 6.5 a.u. In these plots, as R_3 is increased and $R_2\sim 1.83$ a.u., the O–H₂O

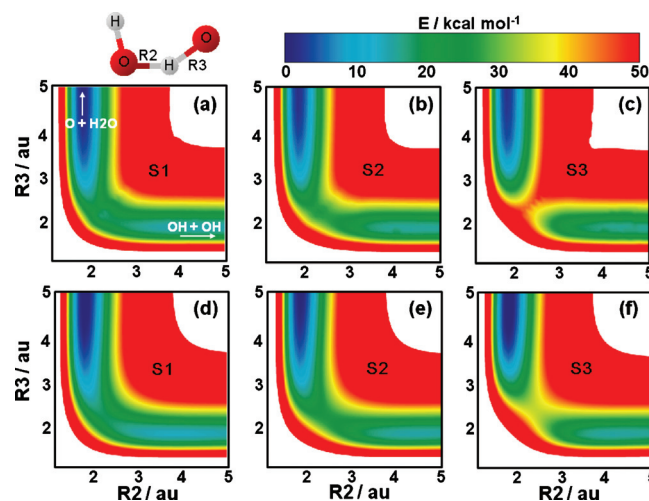


FIG. 3. Contour plots of the $O(^3P)+H_2O(^1A_1)\rightarrow OH(^2II)+OH(^2II)$ reaction. The S1, S2, and S3 state results for the CASSCF+MP2 calculations are given in (a), (b), and (c), respectively. The S1, S2, and S3 state results for the fitted PESs are given in (d), (e), and (f), respectively. The geometry is defined according to the TS1 transition state shown in Fig. 1. The R_2 (abscissa) and R_3 (ordinate) are varied to produce the energy contours. The energy zero corresponds to the equilibrium geometry of the separated $O+H_2O(^1A_1)$ reactants.

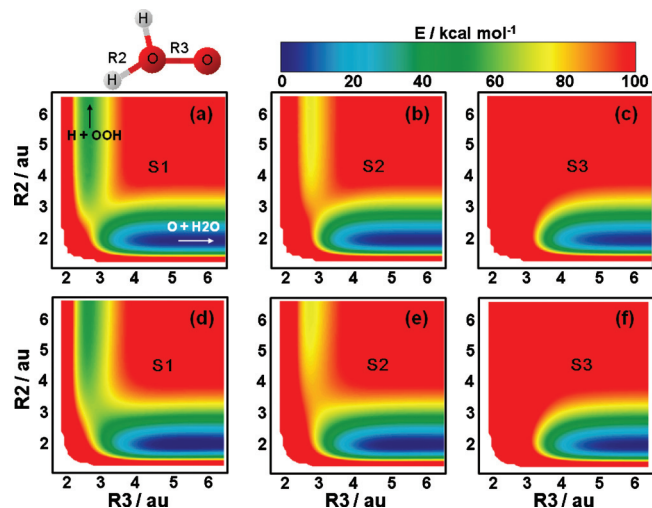


FIG. 4. Contour plots of the $\text{O}(^3\text{P})+\text{H}_2\text{O}(^1\text{A}_1)\rightarrow\text{H}(^2\text{S})+\text{OOH}(^2\text{A})$ reaction. The S1, S2, and S3 state results for the CASSCF+MP2 calculations are given in (a), (b), and (c), respectively. The S1, S2, and S3 state results for the fitted PESs are given in (d), (e), and (f), respectively. The geometry is defined according to the TS5 transition state shown in Fig. 1. The R3 (abscissa) and R2 (ordinate) are varied to produce the energy contours. The energy zero corresponds to the equilibrium geometry of the separated $\text{O}+\text{H}_2\text{O}(^1\text{A}_1)$ reactants.

complex is more reactantlike and as R_2 is increased and $R_3\sim 2.6$ a.u., the complex is more productlike. Overall for the S1 and S2 states, the energy surface is as well characterized using the fitted PES as the *ab initio* calculation. For completeness, we also plot the elimination S3 state for both the CASSCF+MP2 and the PES in Figs. 4(c) and 4(f). No H+OOH local minimum is observed, and the potential is entirely repulsive outside of the $\text{O}+\text{H}_2\text{O}$ reactant state in this configuration for the energies we examined. This is correctly reproduced on the PES.

In Fig. 5, the current fitted surfaces (a)–(c) and our previous fitted surfaces¹² (d)–(f), which do not include the H

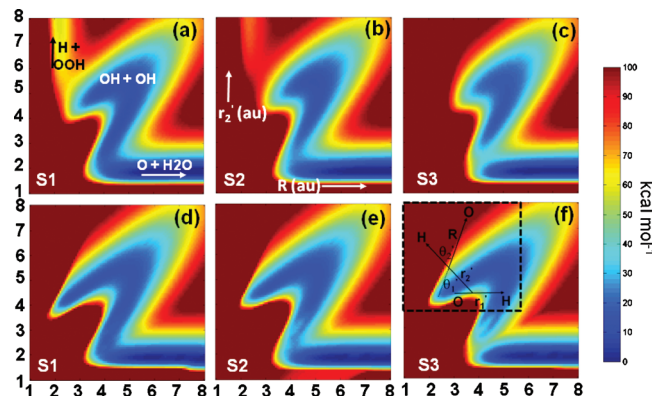


FIG. 5. The potential energy contours in Jacobi coordinates: (a) the S1, (b) the S2, and (c) the S3 electronic states of the PES of the current work; (d) the S1, (e) the S2, and (f) the S3 electronic states of Ref. 12. The triatom Jacobi-like coordinate system of Ref. 26 is used as shown in the inset of (f), where r'_1 is the distance from O atom to H, r'_2 starts from the center of mass of r'_1 , R starts from the center of mass of r'_2 , θ'_1 is the angle between r'_1 and R , and θ'_2 is the angle between r'_2 and R . All atoms are in the same plane, and the inset in (f) is not to scale. From the TS1 geometry given in Fig. 1, $R_1=r'_1=1.83$ a.u., $\theta'_1=84.4^\circ$, and $\theta'_2=22.4^\circ$ are determined. With r'_1 , θ'_1 , and θ'_2 fixed, the coordinates R (abscissa) and r'_2 (ordinate) are then varied to produce the contours.

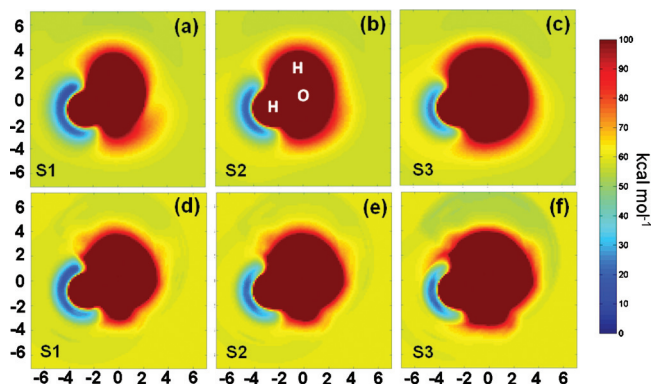


FIG. 6. Potential energy contours of (a) the S1, (b) the S2, and (c) the S3 electronic states of the current work and those of (d) the S1, (e) the S2, and (f) the S3 electronic states of Ref. 12. The reactant H_2O is fixed at the corresponding geometry of TS5 shown in Fig. 1 with the location of the attacking oxygen varying in the plane of the H_2O . Lengths are given in atomic units.

+OOH channel, are compared. In these plots, the triatom atom Jacobi coordinate notation is used²⁶ where each vector is constructed from the center of mass of the previous one as shown in the inset of Fig. 5(f). For large R and small r'_2 , the $\text{O}+\text{H}_2\text{O}$ reactant channel is visible. For small R and large r'_2 , the H+OOH product state is seen. For large R and large r'_2 , the OH+OH is visible. In these coordinates all reactants and products are visible, and the inclusion of the H+OOH channel in the present S1 and S2 surfaces is clearly evident.

The contour plots shown in Fig. 6 compare the three $\text{O}(^3\text{P})+\text{H}_2\text{O}(^1\text{A}_1)$ electronic surfaces for the current work (a)–(c) and our previous PESs (Ref. 12) (d)–(f) in a different set of coordinates. In this figure, the H_2O is fixed at the planar geometry given for TS5 in Fig. 1. The position of the atomic oxygen is varied in the plane of the H_2O . For visualization purposes, the maximum contour shown is 100 kcal mol⁻¹. However, the repulsive potential wall increases to several thousand kcal mol⁻¹ as the O–O distance decreases to approximately 1 a.u. At very small O–O internuclear distances, where no *ab initio* results are available, negative, unphysical values of the fitted potentials did appear. For the classically based dynamics simulations discussed here, these regions can never be accessed. However, for quantum dynamics simulations, it may be necessary to add more *ab initio* points or extra repulsive terms in the fitting procedure. In Fig. 6, the transition state region leading to the OH+OH product is clearly evident in each of the plots as the oxygen atom approaches the hydrogen atom with the longer bond length (2.4 a.u.). As the O-atom approaches this hydrogen, the potential energy decreases to approximately 20 kcal mol⁻¹ (blue contour), which is close to the barrier for the abstraction reaction. The elimination reaction channel is present in Figs. 6(a) and 6(b) as can be seen with a slight 55–70 kcal mol⁻¹ (yellow contour) indentation in the surfaces near the O-atom of the reactant H_2O . In contrast, the previous surfaces (d) and (e) have a repulsive wall blocking the elimination reaction channel. As mentioned above, neither S3 surface has an elimination pathway. The current PESs have a smoother appearance than our earlier work. For example, given the attacking oxygen at the location (–3, 3)

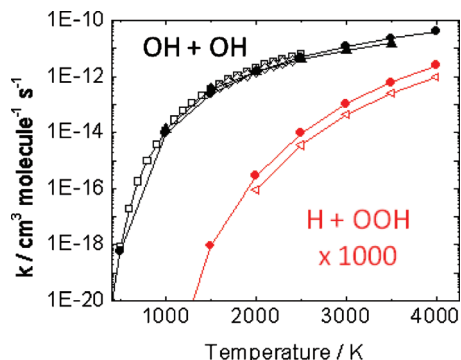


FIG. 7. Rate constants in $\text{cm}^3 \text{molecule}^{-1} \text{s}^{-1}$ as a function of temperature in Kelvin. The hydrogen abstraction reaction is denoted with black lines and the elimination reaction is denoted with red lines. The filled circles are the current work, the filled triangles are the previous results from Ref. 12, the open squares are the experimental results of Ref. 29, the open diamonds are the experimental results of Ref. 28, and the open left triangles are derived from the computational results of Ref. 14. Note that the reaction rates of the elimination reaction are multiplied by 1000 for visualization purposes.

on the S1 surface, the current PES, Fig. 6(a), has a smooth transition from the highly repulsive to less repulsive region. This difference could be due to the fact that the surfaces of Ref. 12 use a spline function designed to go through all the calculated points as opposed to the present procedure which uses basis functions of internuclear distance. The spline-fits, although by definition highly accurate in fitting the *ab initio* points, will be sensitive to the tightness of the convergence of the *ab initio* electronic energies and in regions where the potential changes quickly may require a very high density of points to ensure that the potential is followed smoothly.

III. DYNAMICS RESULTS

A. Rate constants

Variational transition state theory rate constants were calculated for the fitted PESs using POLYRATE.²⁷ Results were obtained over the temperature range of 500–4000 K in steps of 500 K for hydrogen abstraction and 1500–4000 K in steps of 500 K for hydrogen elimination, as shown in Fig. 7. To determine the total rate constant, the contributions from each electronic state are divided by three (the degeneracy factor) then summed together. As mentioned above in the discussion of the surface fit, we assumed no electronic coupling between surfaces, and we have not included quantum corrections to the rate constants. For the abstraction reaction, results using the previous surfaces of Ref. 12 as well two experimental measurements from the literature^{28,29} are also plotted. In general, the agreement between all these results is within a factor of 2 for abstraction. The rate constant results

further validate the barrier height of the abstraction reaction using the PES. For the elimination reaction, the present results are shown along with the results of the calculation of Karkach *et al.*,¹⁴ where each result has been multiplied by 1000 for ease of visualization. The only reported experimental rate constant is at 298 K,³⁰ where it has a value of $10^{-52} \text{ cm}^3 \text{ molecule}^{-1} \text{ s}^{-1}$ compared with the present result of $10^{-56} \text{ cm}^3 \text{ molecule}^{-1} \text{ s}^{-1}$. In Table III, we present the total rate constants for the hydrogen abstraction and elimination reactions determined by the present surfaces and fit to an Arrhenius form.

B. QCT calculations

QCT simulations are performed using the fitted PESs interfaced to the classical trajectory code VENUS.³¹ In the simulations, the initial orientation of the O+H₂O complex was randomly chosen according to Ref. 32 with an initial O–H₂O separation of 17.0 a.u. and a maximum impact parameter of 7.56 a.u. The H₂O molecule is set to the ground vibrational state, i.e., the quantum state of each normal mode is set to the ground state with zero rotational angular momentum. The simulation time step was 1×10^{-16} s and each simulation was run until the reaction product or inelastically scattered reactant separation was 17.0 a.u. 100 000 trajectories were run for each triplet electronic state surface and for each collision energy. The collision energies were 16.2, 25.3, 36.4, 49.6, 64.8, 82.0, 101.2, and 122.5 kcal mol⁻¹, equivalent to collision velocities of 4, 5, 6, 7, 8, 9, 10 and 11 km s⁻¹, respectively. At the highest collision energies, fragmentation of the OOH was possible for elimination reactions, but we did not follow the trajectories long enough in time to observe this.

The total cross sections averaged over the three electronic surfaces for the abstraction (black lines) and elimination (red lines) reactions are plotted as a function of collision energy in Fig. 8(a). For this work (filled circles), the hydrogen abstraction reaction reaches a cross section of approximately 1 a.u. by 64.8 kcal mol⁻¹ (8 km s⁻¹). In contrast, the elimination reaction (red, filled circles) is not observed until 64.8 kcal mol⁻¹. At this collision energy, S1 state trajectories which can borrow some internal energy from the reactant zero point vibration begin to contribute to the cross section. The elimination cross section has a steep increase from threshold, allowing the elimination and abstraction channels to be competitive near 80 kcal mol⁻¹ collision energy, close to the S2 elimination threshold. At the highest collision energy, the cross sections for the two channels are nearly equal. Our previous results¹² (filled triangles) and B3LYP density functional direct dynamics results of Ref. 7 (filled squares) are also plotted in Fig. 8(a). In general, the abstraction cross

TABLE III. Reaction rate constant parameters for the hydrogen abstraction and elimination reactions fit to the Arrhenius equation, $k(T) = A(T/298)^n e^{-E_a/RT}$ for the computed reaction rates in the temperature range of 500–4000 K for OH+OH products and 1500–4000 K for H+OOH products.

Reaction	$A/\text{cm}^3 \text{ molecule}^{-1} \text{ s}^{-1}$	$E_a/\text{kcal mol}^{-1}$	n
$\text{O}(^3\text{P}) + \text{H}_2\text{O}(^1\text{A}_1) \rightarrow \text{OH}(^2\text{II}) + \text{OH}(^2\text{II})$	1.98×10^{-12}	15.9	1.94
$\text{O}(^3\text{P}) + \text{H}_2\text{O}(^1\text{A}_1) \rightarrow \text{H}(^2\text{S}) + \text{OOH}(^2\text{A})$	3.24×10^{-11}	61.6	2.00

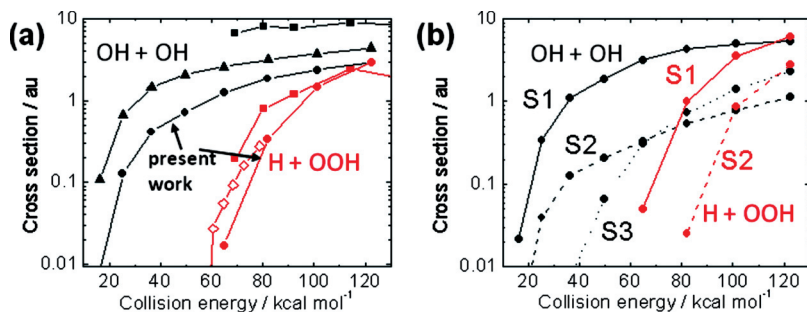


FIG. 8. (a) The total calculated cross sections as a function of collision energy in kcal mol⁻¹ for the hydrogen abstraction reaction (black lines) and hydrogen elimination reaction (red lines). The filled circles are the current work, the filled triangles are the previous results from Ref. 12, the filled squares are the computational results of Ref. 7, and the open diamonds are the experimental results of Ref. 7. (b) The unweighted state resolved abstraction (black) and elimination (red) cross sections for the S1 state (solid lines), S2 state (dashed lines), and S3 state (dotted lines).

section from the current work is approximately a factor of 1.5 less than our previous calculations¹² at the highest collision energies studied. We will discuss the factors affecting the cross section differences for these surfaces in greater depth below. The B3LYP OH+OH direct dynamics result of Ref. 7 is approximately a factor of 4 greater than the cross section of the present work. This may be due to the fact that the direct dynamics simulation of Ref. 7 has a lower barrier for the OH reaction channel compared to the present PES. In Ref. 7, the reaction barrier is not directly given but approximated as the OH reaction energy, 14.6 kcal mol⁻¹ (11.8 kcal mol⁻¹ including zero point energy). Zheng *et al.*³³ have also previously noted the underestimation in barrier height using B3LYP. The differences between the cross sections may also be due to the electronic state averaging in the present simulations, which may not have been taken into account in the B3LYP single surface results. For the hydrogen elimination reaction (red lines), the results of the current work (filled circles) are plotted with the B3LYP computation (filled squares) and experimental results (open diamonds) of Ref. 7 in Fig. 8(a). Near threshold, where the cross section is low and steeply rising, there is a factor of ~ 5 difference between the present results and the B3LYP results. This difference diminishes until at 120 kcal mol⁻¹ both results have nearly the same value. The experimental results are scaled with a constant factor to match our current computational elimination cross section results at approximately 64.8 kcal mol⁻¹. There is good agreement between the steep rise near threshold of the experimental and both theoretical results. For the present calculations, the cross section statistical uncertainty is fairly small, with a standard deviation of approximately 0.003 a.u. near the reaction thresholds and 0.01–0.06 a.u. at the highest collision energies.

The current cross sections of the hydrogen abstraction (black lines) and elimination (red lines) reactions separated into electronic state contributions are shown in Fig. 8(b), without the factor of 1/3 used to state average the results

shown in Fig. 8(a). The S1 state results are plotted with solid lines, the S2 results are plotted with dashed lines, and the S3 results are plotted with dotted lines. The S2 begins to contribute to the elimination cross section above 82 kcal mol⁻¹, or 9 km s⁻¹, in accordance with the activation barrier for this reaction on this excited surface. By 122.5 kcal mol⁻¹, the S2 state elimination cross section is approximately half of the S1 state. For the hydrogen abstraction cross section, the S1 state is the largest contributor throughout the range of collision energies examined. While there is an appreciable abstraction cross section for the S2 state, it is approximately a factor of 5 less than the abstraction S1 state. For the S3 state at collision energies below 64.9 kcal mol⁻¹ (8 km s⁻¹), the abstraction cross section is lower than the abstraction cross section for S2 state. Above that energy, the S3 abstraction cross section increases dramatically and becomes an appreciable part of in the total cross section.

The competition between the reactive pathways and, in particular, the role of the S3 surface in the abstraction reaction at high collision energies can be further examined through the opacity function, $P(b)$. The opacity function has the following relation to the total reactive cross section: $\sigma = 2\pi \int_0^{b_{\max}} P(b) b db$, where b is the impact parameter. In Fig. 9(a), the opacity functions for the abstraction (black) and elimination (red) reactions are plotted versus impact parameter in a.u. using the current PESs at the highest collision energy examined, 122.5 kcal mol⁻¹. Near-zero impact parameters b correspond to O-atom attack on the H₂O O-atom and geometries which favor the elimination channel. Impact parameters of 2.0 a.u. and greater correspond to O-atom approaches toward the H₂O hydrogens, which favor the abstraction channel. The S1 state results are plotted with solid lines, the S2 results are plotted with dashed lines, and the S3 results are plotted with dotted lines. For the S1 and S2 surfaces, as the impact parameter becomes smaller than 2 a.u., there is an increasing probability of reaction for the elimina-

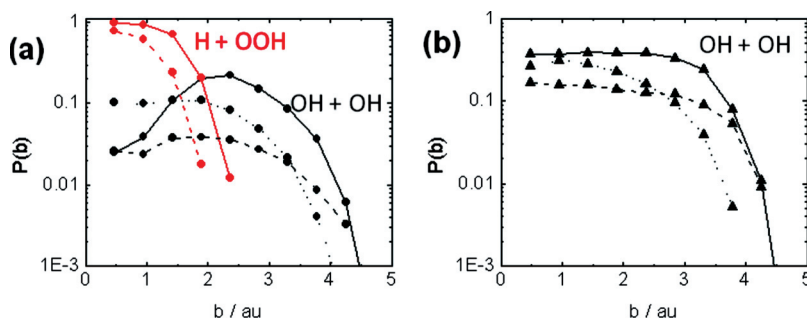


FIG. 9. (a) Opacity functions for the hydrogen abstraction (black) and elimination (red) reactions plotted vs impact parameter in atomic units. The S1 state is shown in solid lines, the S2 state is shown in dashed lines, and the S3 state is shown in dotted lines. (b) Opacity function for the hydrogen abstraction reaction for our previous simulation, Ref. 12, plotted vs impact parameter in atomic units. The S1 state is the solid line, the S2 state is the dashed line, and the S3 state is the dotted line.

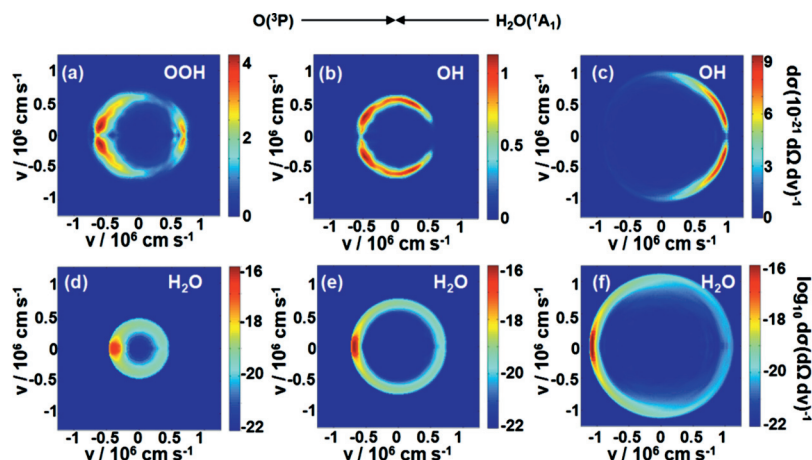


FIG. 10. Velocity-flux contours $d\sigma(d\Omega dv)^{-1}$, in units of $\text{cm}^2 (\text{sr cm s}^{-1})^{-1}$. (a) The differential cross section of the OOH elimination product at collision energy of $122.5 \text{ kcal mol}^{-1}$. (b)–(c) The differential cross section active OH product (formed from the attacking O-atom) at a collision energies of 49.6 and $122.5 \text{ kcal mol}^{-1}$, respectively. (d)–(f) The differential cross sections of H₂O for nonreactive O(³P)+H₂O(¹A₁) collisions at energies of 16.2 , 49.6 , and $122.5 \text{ kcal mol}^{-1}$, or collision velocities of 4 , 7 , and 11 km s^{-1} , respectively. Note in (d)–(f) the contour scale is logarithmic.

tion reaction. For the abstraction reaction, the opacity function decreases with impact parameters less than 2 a.u. for the S1 and S2 states, and remains constant on the S3 surface. A significant probability for the abstraction reaction with small parameters on the S3 surface is the result. At larger impact parameters, especially between 2 and 3 a.u. for the S1 surface, more glancing collisions are likely which favor the hydrogen abstraction reaction. The opacity function also highlights the differences between our previous¹² and current calculation of the OH cross section shown in Fig. 8(a). In Fig. 9(b), the opacity function is given versus impact parameter using our previous OH+OH trajectories at $122.5 \text{ kcal mol}^{-1}$.¹² Since the elimination reaction is not included in the previous PESs, the abstraction reaction probability is significant at impact parameters below 2 a.u. on the S1 and S2 surfaces. Therefore, a larger total cross section for the OH reaction channel is obtained in our previous results at these high energies.

In addition to the opacity functions, flux-velocity contour maps provide insight into the competition between abstraction and elimination channels as well as direct collisional excitation of H₂O. They may also be used as a guide for future hyperthermal measurements of the O+H₂O collision system. Flux (velocity-angle) contour maps constructed from the present QCT simulations are given in Fig. 10, where the differential cross sections [in units of $\text{cm}^2 (\text{sr cm s}^{-1})^{-1}$] are given as a function of velocity in cm s^{-1} in a center of mass system where the origin corresponds to zero kinetic energy of the collision products. In Fig. 10(a), the flux contour of the OOH radical is shown at a collision energy of $122.5 \text{ kcal mol}^{-1}$ (11 km s^{-1}). A majority of the OOH back scatter toward the atomic oxygen as would be expected from direct O-atom attack on the H₂O O-atom. Similar flux for the elimination channel was observed in the direct dynamics calculations of Schatz and Minton.⁷ In Figs. 10(b) and 10(c), the flux is given for the “active” OH product in the abstraction pathway, which contains the attacking atomic oxygen. At a collision energy of $49.6 \text{ kcal mol}^{-1}$ [Fig. 10(d)], the OH product tends to back and side scatter which is expected from the transition geometry of TS1. However at a higher collision energy of $122.5 \text{ kcal mol}^{-1}$, Fig. 10(c), the active OH forward scatters. This scattering angle can be attributed to a “stripping”

mechanism as had previously been identified for high energy O–H abstraction reactions.^{10,34} At $122.5 \text{ kcal mol}^{-1}$, we note that the OOH backscatters while the OH forward scatters. In addition to the reactive channels, inelastically scattered H₂O will play a significant and perhaps dominant role in the radiation observed in O+H₂O collisions. In (d)–(f), we present differential cross sections of inelastically scattered H₂O on a log scale with respect to the velocity components at collision energies of 16.2 , 49.6 , and $122.5 \text{ kcal mol}^{-1}$, equivalent to collision velocities of 4 , 7 , and 11 km s^{-1} , respectively. As expected, there is a large number of near miss, low scattering angle trajectories (red contour). However, there is also significant collisional excitation. For example at $16.2 \text{ kcal mol}^{-1}$, where the reactive cross section is low as shown in Fig. 8(a), many of the trajectories with small impact parameters and large scattering angles will inelastically collide and excite the H₂O. This internal excitation is shown in Fig. 10(d) with a distribution of cross sections at various radii from the origin. For example, at this collision energy, the total cross section for H₂O with internal energies greater than 20 kcal mol^{-1} is 9.1 a.u. Likewise at the higher collision velocities shown in Figs. 10(e) and 10(f), there is a distribution of H₂O cross sections at various translational radii which gives rise to internally excited H₂O. In comparison to the lower $16.2 \text{ kcal mol}^{-1}$ collision energies, the total cross section for H₂O with internal energies greater than 20 kcal mol^{-1} are 28.1 and 37.9 a.u. for collision energies of 49.6 and $122.5 \text{ kcal mol}^{-1}$, respectively. A detailed examination of the internal energy distributions of scattered H₂O, OH, and OOH will be presented in future work.

IV. CONCLUSIONS

Electronic structure calculations were performed at the CASSCF+MP2 level with an O($4s3p2d1f$)/H($3s2p$) one electron basis set on the O(³P)+H₂O(¹A₁) collision system. Approximately 10^5 geometries were used to fit the three lowest triplet adiabatic states corresponding to the triply degenerate reactants. The method of Bowman and co-workers,^{16,17} which includes all nuclear degrees of freedom, and where the interchangeability of like-atoms is built into the functional form of the potential, was used to fit the *ab initio* points. Each surface is treated independently. The OH+OH

abstraction and H+OOH elimination reactions were included in the surface fits. With these fitted surfaces, variational transition state theory was used to determine rate constants leading to OH+OH and H+OOH which compare favorably to literature values. We have also computed cross sections using quasiclassical trajectories for production of OH+OH and H+OOH from threshold to ~ 120 kcal mol⁻¹ (~ 11 km s⁻¹). For the OH+OH channel, the present results are about a factor of 4 lower than those reported by Brunsvold *et al.* using B3LYP density functional direct dynamics on a single surface and about a factor of 2 lower than our previous results¹² which used fitted surfaces only for the OH+OH channel. For the H+OOH channel the present results are about a factor of 4 less than the B3LYP direct dynamics cross sections of Brunsvold *et al.*⁷ at threshold and are similar at higher energies. The present H+OOH results have good agreement with molecular beam measurements⁷ for the relative cross section. We have also examined the opacity function for reaction on each of our fitted surfaces. These opacity functions highlight large differences in the contributions of each of the electronic triplet states, especially at higher energies where the OH+OH and H+OOH channels are competitive. Finally, we have determined flux-velocity contour maps at selected energies leading to H₂O collisional excitation, OH+OH, and H+OOH. These maps show the large differences in angular scattering and mechanism between the two reactive channels, and may also serve as a guide to future hyperthermal laboratory measurements of these quantities. Taken together, we believe the present surfaces should be able to quantitatively model O+H₂O collision processes from threshold to ~ 120 kcal mol⁻¹ and probably up to 150 kcal mol⁻¹. Future work will investigate the detailed dynamics and product distributions using these surfaces.

ACKNOWLEDGMENTS

P.F.C. and M.B. acknowledge support under Contract No. FA8718-05-C-0077.

- ¹D. K. Zhou, W. R. J. Pendleton, G. E. Bingham, and A. J. Steed, *Geophys. Res. Lett.* **21**, 613 (1994); D. K. Zhou, W. R. J. Pendleton, G. E. Bingham, D. C. Thompson, W. J. Raitt, and R. M. Nadile, *J. Geophys. Res.* **99**, 19585 (1994).
- ²R. E. Meyerott, G. R. Swenson, and E. L. Schweitzer, *J. Geophys. Res.* **99**, 17559 (1994).
- ³L. S. Bernstein, J. B. Elgin, C. P. Pike, D. J. Knecht, E. Murad, T. F. Zehnpfennig, G. E. Galicia, and A. T. J. Stair, *J. Geophys. Res.* **101**, 383 (1996); D. L. A. Rall, I. L. Kofsky, C. P. Pike, D. J. Knecht, and T. F. Zehnpfennig, *J. Spacecr. Rockets* **33**, 393 (1996).
- ⁴L. S. Bernstein, Y.-H. Chiu, J. A. Gardner, A. K. Broadfoot, M. I. Lester, M. Tsiouris, R. A. Dressler, and E. Murad, *J. Phys. Chem. A* **107**, 10695 (2003); L. S. Bernstein, M. Braunstein, A. K. Broadfoot, W. L. Dimpfl, R. A. Dressler, Y.-H. Chiu, J. A. Gardner, and E. Murad, *J. Spacecr. Rockets* **43**, 1370 (2006).
- ⁵B. Ruscic, A. F. Wagner, L. B. Harding, R. L. Asher, D. Feller, D. A.

- Dixon, K. A. Peterson, Y. Song, X. Qian, C.-Y. Ng, J. Liu, W. Chen, and D. W. Schwenke, *J. Phys. Chem. A* **106**, 2727 (2002).
- ⁶B. Ruscic, R. E. Pinzon, M. L. Morton, N. K. Srinivasan, M.-C. Su, J. W. Sutherland, and J. V. Michael, *J. Phys. Chem. A* **110**, 6592 (2006).
- ⁷A. L. Brunsvold, J. M. Zhang, H. P. Upadhyaya, T. K. Minton, J. P. Camden, J. T. Paci, and G. C. Schatz, *J. Phys. Chem. A* **111**, 10907 (2007).
- ⁸O. J. Orient, A. Chutjian, and E. Murad, *Phys. Rev. Lett.* **65**, 2359 (1990).
- ⁹M. G. Dunn, G. T. Skinner, and C. E. Treanor, *AIAA J.* **13**, 803 (1975).
- ¹⁰D. Troya, R. Z. Pascual, and G. C. Schatz, *J. Phys. Chem. A* **107**, 10497 (2003).
- ¹¹D. Troya, M. Mosch, and K. A. O'Neill, *J. Phys. Chem. A* **113**, 13863 (2009).
- ¹²M. Braunstein, R. Panfili, R. Shroll, and L. Bernstein, *J. Chem. Phys.* **122**, 184307 (2005).
- ¹³B. R. Johnson, *J. Chem. Phys.* **84**, 176 (1986); M. J. Redmon, G. C. Schatz, and B. C. Garrett, *ibid.* **84**, 764 (1986).
- ¹⁴S. P. Karkach and V. I. Osherov, *J. Chem. Phys.* **110**, 11918 (1999).
- ¹⁵M. W. Schmidt, K. K. Baldrige, J. A. Boatz, S. T. Elbert, M. S. Gordon, J. H. Jensen, S. Koseki, N. Matsunaga, K. A. Nguyen, S. J. Su, T. L. Windus, M. Dupuis, and J. A. Montgomery, *J. Comput. Chem.* **14**, 1347 (1993).
- ¹⁶C. Chen, B. C. Shepler, B. J. Braams, and J. M. Bowman, *J. Chem. Phys.* **127**, 104310 (2007); X. Huang, B. J. Braams, and J. M. Bowman, *ibid.* **122**, 044308 (2005); W. K. Park, J. Park, S. C. Park, B. J. Braams, C. Chen, and J. M. Bowman, *ibid.* **125**, 081101 (2006).
- ¹⁷B. J. Braams and J. M. Bowman, *Int. Rev. Phys. Chem.* **28**, 577 (2009).
- ¹⁸*NIST Chemistry WebBook, NIST Standard Reference Database Number 69*, edited by P. J. Linstrom and W. G. Mallard (National Institute of Standards and Technology, Gaithersburg, MD, 2010).
- ¹⁹S. Matsika and D. R. Yarkony, *J. Chem. Phys.* **117**, 3733 (2002).
- ²⁰R. Sayós, C. Olivia, and M. Gonzales, *J. Chem. Phys.* **115**, 8828 (2001).
- ²¹S. Garashchuk, V. A. Rassolov, and G. C. Schatz, *J. Chem. Phys.* **124**, 244307 (2006).
- ²²S. Takahashi, R. Wada, Y. Matsumi, and M. Kawasaki, *J. Phys. Chem.* **100**, 10145 (1996).
- ²³H. Partridge and D. W. Schwenke, *J. Chem. Phys.* **106**, 4618 (1997).
- ²⁴G. M. Thurman and R. Steckler, *J. Phys. Chem. A* **105**, 2192 (2001).
- ²⁵K. P. Huber and G. Herzberg, *Constants of Diatomic Molecules* (Can Nostrand, Princeton, 1979).
- ²⁶F. Gatti, *J. Chem. Phys.* **111**, 7225 (1999); J. Mayneris, M. Gonzales, and S. K. Gray, *Comput. Phys. Commun.* **179**, 741 (2008).
- ²⁷J. C. Corchado, Y.-Y. Chuang, P. L. Fast, J. Villa, W.-P. Hu, Y.-P. Liu, G. C. Lynch, K. A. Nguyen, C. F. Jackels, V. S. Melissas, B. J. Lynch, I. Rossi, E. L. Coitino, A. Fernandez-Ramos, J. Pu, T. V. Albu, R. Steckler, B. C. Garrett, A. D. Isaacson, and D. G. Truhlar, *POLYRATE-v9.3* (University of Minnesota, Minneapolis, 2002).
- ²⁸A. M. Lifschitz and J. V. Michael, *Sym. (Int.) Combust., [Proc.]* **23**, 56 (1991).
- ²⁹W. Tsang and R. F. Hampson, *J. Phys. Chem. Ref. Data* **15**, 1087 (1986).
- ³⁰W. Hack, A. W. Preuss, H. G. Wagner, and K. Hoyermann, *Ber. Bunsenges. Phys. Chem.* **83**, 212 (1979).
- ³¹W. L. Hase, R. J. Duchovic, X. Hu, A. Komornicki, K. F. Lim, D.-h. Lu, G. H. Peshlherbe, K. N. Swamy, S. R. Vande Linde, A. Varandas, H. Wang, and R. J. Wolf, *VENUS96: A General Chemical Dynamics Program* Quantum Chemistry Program Exchange, 16, 671 (1996).
- ³²W. L. Hase, D. M. Ludlow, R. J. Wolf, and T. Schlick, *J. Phys. Chem.* **85**, 958 (1981).
- ³³J. Zheng, Y. Zhao, and D. G. Truhlar, *J. Chem. Theory Comput.* **3**, 569 (2007).
- ³⁴J. C. Polanyi, *Acc. Chem. Res.* **5**, 161 (1972); T. Y. Yan, C. Doubleday, and W. L. Hase, *J. Phys. Chem. A* **108**, 9863 (2004); J. M. Zhang, D. J. Garton, and T. K. Minton, *J. Chem. Phys.* **117**, 6239 (2002).